Volume 4
Number 3
March 2026
Pages 1117–1636

RSC Sustainability

rsc.li/rscsus

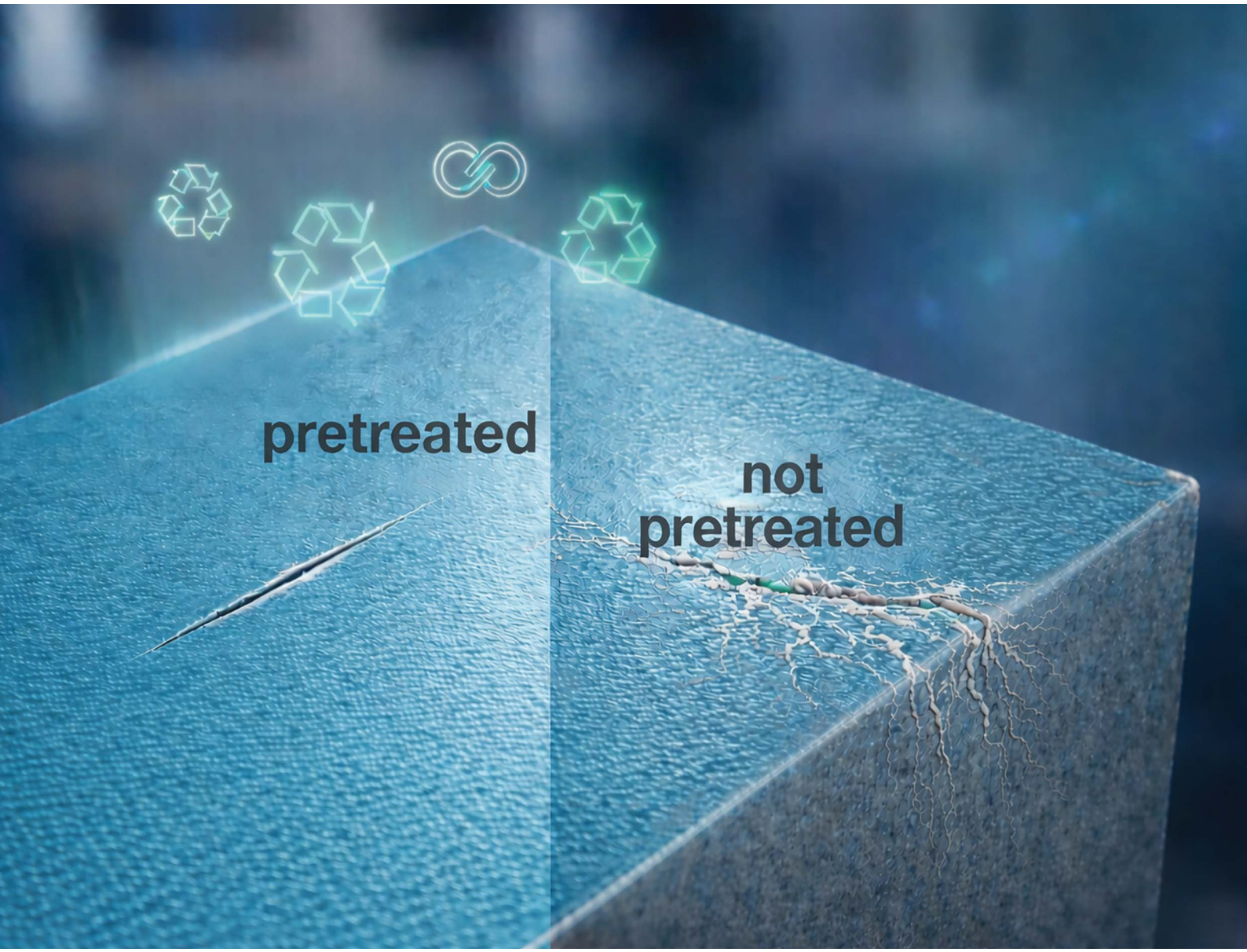

ISSN 2753-8125

ROYAL SOCIETY OF CHEMISTRY

PAPER
Erlind Mysliu, Malgorzata Chojak Halseid, Andreas Erbe *et al.*
Primary-equivalent corrosion protection of post-consumer scrap based aluminium

RSC Sustainability

ROYAL SOCIETY OF CHEMISTRY

PAPER

View Article Online
View Journal | View Issue

Cite this: *RSC Sustainability*, 2026, **4**, 1367

Primary-equivalent corrosion protection of post-consumer scrap based aluminium

Erlind Mysliu,†*[a] John Erik Lein,[b] Per Erik Vullum,[b] Jan Tore Buvik Gundersen,[c] Malgorzata Chojak Halseid,*[c] Otto Lunder[b] and Andreas Erbe *[a]

Will increased amount of post-consumer scrap in aluminium increase the susceptibility of powder-coated aluminium alloys towards filiform corrosion? An answer to this so far unanswered question is crucial for large scale industrial implementation of post-consumer scrap based aluminium. Systematic variation of the pretreament consisting of different variants of alkaline etching, acidic oxidising desmutting, and conversion coating shows that variation between specimens depends on details of extrusion processes and oxide thickness instead of initial composition of 6060 aluminium alloys. Excessive Mg surface enrichment, as evidenced through glow discharge optical emission spectroscopy and transmission electron microscopy, prevents formation of ZrO_2 conversion coatings, requiring adaption of pretreatment processes. The observed Mg enrichment is unrelated to recycling. Industrial standardised tests for filiform corrosion according to a Qualicoat standard reveal that after alkaline etching of 2 g m^{-2} using standard process chemicals, alloys with Cu and Zn content of up to ≈0.035 mass% fulfil industrial filiform corrosion resistance requirements. The content of Cu and Zn is above the currently considered industrial limit of 0.02 mass%; the exact upper limit of alloy element content has not been investigated in this study. According to results obtained here, increasing amount of post-consumer scrap will not increase susceptibility towards filiform corrosion. Hence, associated industrial standards should orient on performance and not arbitrarily limit alloy composition. Performance-oriented standards could become enablers for increased sustainability of materials production.

Received 18th May 2025
Accepted 9th December 2025

DOI: 10.1039/d5su00350d

rsc.li/rscsus

Sustainability spotlight

United Nations Sustainable Development Goal (SDG) 12 – Responsible Consumption and Production includes to "reduce waste generation through prevention, reduction, recycling and reuse". Increased use of recycled aluminium based on post-consumer scrap (PCS) is an integral part of SDG 12, requiring industrial scale solutions. Industrial aluminium recycling of PCS can yield alloys with a slightly larger amounts of copper, iron and zinc. These elements play an important role in aluminium corrosion, so that concerns about corrosion in PCS-based aluminium exist. This work shows mechanisms through which – with appropriate pretreatment using already available solutions – industrial grade PCS-based coated aluminium with larger content of alloy elements than currently considered industrially feasible fulfils industrial requirements.

1 Introduction

Aluminium recycling is one of the most promising industrial processes for reducing CO_2 emissions, since recycling requires only 5% of the energy required to produce aluminium from bauxite.[1] For example, the aluminium demand generated by the construction of large-scale photovoltaic power plants has the potential to lead to strong contributions to CO_2 emissions unless met by recycled aluminium.[2] Wider adoption of aluminium is positive from a sustainability perspective,[3,4] and requires, amongst others, appropriate supply chain management.[5] Increased aluminium recycling builds on knowledge about the properties of PCS-based aluminium.[6] Non-selective collection of PCS is a major obstacle in preventing down-cycling.[7] Collecting clean scrap enables use of PCS-based aluminium even for highly demanding aerospace applications.[8]

Although highly advanced scrap sorting technologies enable reasonable control over alloy composition on the industrial scale,[9–11] certain elements may enrich during recycling. When elements more noble than aluminium, such as Cu, are present in aluminium alloys, the corrosion susceptibility can increase because of the possibility of galvanic coupling between intermetallic particles (IMPs) and the less noble matrix. Increasing Cu and Si levels affect the atomic structure of IMPs.[12] Adverse

[a]*Department of Materials Science and Engineering, NTNU, Norwegian University of Science and Technology, 7491 Trondheim, Norway. E-mail: ffc-tests-al@the-passivists.org*

[b]*SINTEF Industry, 7465 Trondheim, Norway. E-mail: erlind.mysliu@sintef.no*

[c]*R&D Centre, Hydro Aluminium Metal, Hydroveien 160, 4265 Håvik, Norway. E-mail: malgorzata.halseid@hydro.com*

† Present address: SINTEF Industry, 7465 Trondheim, Norway.

effects of Cu can be compensated for by Ce,[13] a rare and expensive alloy element.

For coated aluminium, IMP – matrix galvanic coupling can increase the susceptibility to filiform corrosion (FFC).[14,15] FFC is the main underpaint corrosion mechanism on aluminium.[15,16] FFC initiates from coating defects and edges. Worm-like filaments propagate at certain locations at the metal/coating interface. The cathodic aluminium oxidation occurs usually at the acidic head, where as cathodic activity in the tail is driving propagation. Details of the mechanisms are discussed elsewhere.[15–17] Mitigation strategies may involve release of specific inhibitors that act in acidic solutions.[18]

In some studies, the presence of an increased amount of Cu in recycled aluminium alloys did not have a negative effect on the corrosion susceptibility,[19] even though (i) IMPs play a role in the FFC mechanism,[15,20,21] and (ii) solute atoms play a major role in the dissolution mechanism of aluminium metal.[22] A relatively high Cu surface enrichment is also not reflected in a decreased FFC resistance.[23] Appropriate heat treatment can be used to achieve both sufficient mechanical properties and corrosion resistance.[24] Higher general corrosion rates of secondary aluminium in certain media have been exploited for hydrogen production,[25] which may not be the most efficient materials usage strategy. For certain alloy classes, such as Si-rich cast alloys with higher total amount of alloy elements,[26] there is less concern over a possible loss of corrosion resistance compared to, *e.g.*, extruded alloys with lower content of alloy elements.

Large scale implementation of PCS-based aluminium, *e.g.*, in buildings, requires reliable data on the effect of different pretreatments on the FFC susceptibility. Some industrial producers and end users are still sceptical towards using PCS-based alloys due to the possibly relatively high amount of noble elements deriving from the recycling process. Although there is an indication of a negative effect of increasing Cu content, different cases have demonstrated that the choice of surface preparation or coating plant has a greater impact on corrosion susceptibility than alloy composition.[27,28] Likewise, our mechanistic and performance studies of alkaline etching[29] and conversion coating[23] did not evidence characteristic differences between primary and PCS-based secondary alloys. To enable informed decisions about the properties of PCS-based aluminium, it is important to investigate the effect of different surface treatments on the FFC susceptibility. Relevant data on PCS-based aluminium is to our knowledge not available in the literature.

Table 1 Elemental composition, in mass%, of the three 6060 aluminium alloy variants tested for FFC. Balance Al. The composition of variants C5 and C5b is very similar but the variants have been extruded at two different sites and the billets were cast at different times

Element	C1	C5	C5b
Si	0.48	0.45	0.50
Fe	0.20	0.20	0.21
Cu	0.036	0.029	0.031
Mn	0.039	0.040	0.044
Mg	0.35	0.36	0.36
Cr	0.005	0.006	0.0078
Ni	—	—	0.0061
Zn	0.23	0.030	0.032
Ti	0.019	0.015	0.016
Pb	0.003	0.003	0.0028

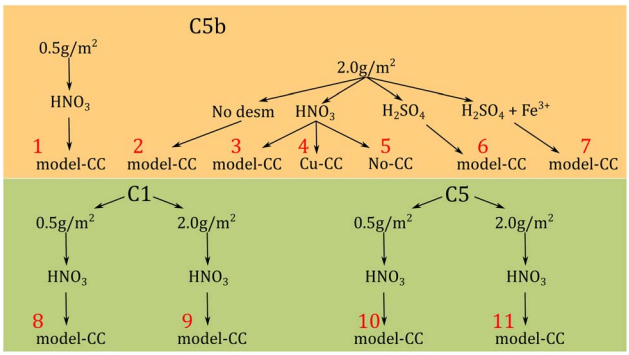

Fig. 1 Different surface pretreatment steps used in this work for 6060 aluminium alloy variants C5b, C1 and C5 before powder coating and FFC testing. Variant C5b was extruded at a different extrusion plant with different die, comparing to samples C1 and C5. Samples were first alkaline etched to remove either 0.5 g m^{-2} or 2 g m^{-2} material. Subsequently, samples were desmutted using one of three different acidic oxidisers [HNO_3, H_2SO_4 or H_2SO_4 + $Fe_2(SO_4)_3$]. Next, ZrO_2-based conversion coatings (CCs) were applied, either using pure H_2ZrF_6 as precursor (model-CC), a bath also containing $Cu(NO_3)_2$ as accelerator (Cu-CC); selected samples received no CC (No-CC). Finally, samples were powder coated using a polyester coating. Not all the possible sample/surface combinations were prepared based on experience from other experiments. The red numbers indicate the name of a certain sample set and surface pretreatment used for reference in the text.

In this work, FFC tests on recycled aluminium alloys based on >75% PCS were performed to determine the effect of surface pretreatment on the FFC performance of three alloy variants (Table 1). Alloy composition was similar to typical 6060 aluminium alloys, one variant with a Cu : Zn mass ratio of ≈1.5 and two variants with ≈1. Billets were extruded and the resulting profiles were alkaline etched, desmutted and conversion coated (Fig. 1). Finally, samples were powder coated and then subjected to FFC tests according to an industry standard.[30] An overview over the surface pretreatments and samples is shown in Fig. 1.

Selected samples were analysed at different stages. Glow discharge optical emission spectroscopy (GD-OES) was used to determine element concentration profiles in the first micrometers. Different techniques in transmission electron microscopy (TEM) of cross-sections were used to relate surface treatment effects to FFC susceptibility. Elemental maps were obtained in scanning TEM (STEM) mode using energy dispersive X-ray spectroscopy (EDX) and electron energy loss spectroscopy (EELS). Data associated with this study is available online.[31]

2 Materials and methods

2.1 Materials and sample preparation

Three alloy variants were used for this work. Their composition is shown in Table 1.

The overall treatment variation used in this study is shown in Fig. 1. All samples were degreased in acetone and ethanol prior

to any other treatment. Subsequently, samples were rinsed with deionised water. The first pretreatment step was alkaline etching in a 2.5 M NaOH bath at 60 °C in order to remove 0.5 or 2 g m^{-2} of the surface. After the alkaline etching step, all samples were rinsed with deionised water. The second pretreatment step was desmutting in an acidic solution. For this step four different variants of desmutting were used, (i) concentrated HNO_3 (68%), (ii) H_2SO_4 (150 g L^{-1} of concentrated sulphuric acid), (iii) a combination of H_2SO_4 and Fe^{3+} [82 mL of H_2SO_4 (97%) + 5 g $Fe_2(SO_4)_3$], and (iv) no desmutting. The last pretreatment step was the application of a ZrO_2-based CC. Three different combinations were used, (i) a CC based on H_2ZrF_6 (<200 mg L^{-1} of Zr) containing <50 mg L^{-1} of Cu^{2+} (Cu-CC), (ii) a CC prepared with H_2ZrF_6 (<200 mg L^{-1} of Zr) but additive-free (model-CC), and (iii) no CC. The CC was applied by immersion of the sample in the conversion bath for 120 s and subsequent rinsing with deionised water.

Accelerated FFC tests were performed according to Qualicoat specifications[30] after powder coating the samples with a *ca.* 70–90 μm thick polyester coating. Corrosion was initiated by dripping 37% HCl in an artificially created defect using a Sikkens scribe tool. After 1 minute, the 37% HCl was wiped away with laboratory paper and the samples were left for 60 minutes at room temperature. The samples were then transferred into a climatic chamber and left at 40 °C and 82% relative humidity for 1000 hours. During FFC tests, three parallels of each sample/surface pretreatment combination were used.

The susceptibility to FFC was evaluated by measuring the longest filament and the most frequent filament length *M*. From these measurements, the filament number *F* was calculated as $F = H \times M$, where *H* is the filament density $\left(\frac{\text{number of filaments}}{\text{length of scratch}}\right)$. The length of the longest filament was determined by measuring the distance between the artificial defect and the tip of the filament. The most frequent filament length was calculated by measuring the distance to which the majority of filaments developed from the scribes. Maximum filament length and most frequent filament length were evaluated by measuring the length of the filaments on both sides of the scratches/coating defect.

After FFC testing, the coating was removed by exposing the samples to acetone for 24 hours. Samples from sets 1, 3, 7, 10, and 11 were used for GD-OES analysis. Samples from sets 1, 3, and 10 were used for TEM analysis.

2.2 Characterisation methods

2.2.1 GD-OES. GD-OES surface characterization was performed using a Horiba GD-Profiler 2 with an argon plasma source. Source parameters were 32 W applied power and argon pressure of 600 Pa. Before analysis, the GD-OES source was flushed for 90 s.

2.2.2 TEM. TEM samples were prepared by focused ion beam, using a Helios G4 UX instrument from Thermo Fisher Scientific (former FEI). A thick carbon protection layer was first deposited on top of the region of interest. The first part of this layer was deposited by electron beam assisted deposition to avoid any potential Ga^+ ion beam damage to the sample surface. Samples were transferred to a dedicated Cu half-grid by a standard lift-out technique, using a tungsten "Easylift" micromanipulator to transfer the cut-out lamellae. All coarse thinning was performed at 30 kV acceleration voltage for the Ga^+ ions. Final thinning was performed first at 5 kV and then 2 kV on either side of the lamellae to minimize surface damage.

TEM was performed with a double spherical aberration corrected, cold FEG JEOL ARM 200FC, operated at 200 kV. All spectroscopy was performed in scanning transmission electron microscopy (STEM) mode. Energy dispersive X-ray spectroscopy (EDX) was performed with a large solid angle (covering 0.98 sr solid angle), 100 mm^2 Centurio detector, while electron energy loss spectroscopy (EELS) was performed simultaneously with a GIF Quantum ER spectrometer.

3 Results

3.1 Corrosion tests

Despite the typically high uncertainty of FFC tests, some trends are visible from the evaluation of the longest filament and the filament number (Fig. 2). Samples of variant C5b etched for 0.5 g m^{-2} have a higher FFC susceptibility compared to samples etched 2 g m^{-2}. For variants C1 and C5, such a performance difference was not observed.

There is no clear indication of any desmutting method leading to better performance, considering the uncertainty. Samples desmutted in H_2SO_4 and Fe^{3+}, in concentrated HNO_3, in H_2SO_4 and without desmutting have a very similar performance for variant C5b. For C1 and C5 the effect of desmutting was not systematically evaluated and would require more extensive tests.

The large sample-to-sample variation makes it difficult to quantitatively assess the performance of a certain CC system with respect to others if only the longest filament and the most frequent filament length are considered. The filament number gives in certain cases a better indication of the FFC susceptibility. For variant C5b, there are fewer filaments with CC though their length is similar both with and without CC. The performance after applying a model-CC or Cu-CC is comparable. In analogy to the case of desmutting, for variants C1 and C5 the same CC system was used for the two different measurements. Therefore, the effect of the CC cannot be evaluated for these variants.

3.2 Interfacial analysis

GD-OES analyses of the as prepared samples (Fig. 3a and b) show a surface enrichment of Mg and Cu. Although the bulk sample composition is similar, the distribution of the surface enrichment differs remarkably. The maximum amount of Cu is very similar for all three samples, but the total enriched amount obtained from the peak area is highest for variant C5b. Additionally, Cu surface enrichment for C5b is located deeper in the sample. Analogously, the Mg enrichment for variant C5b is located at greater depths, but in this case the maximum enrichment is approximately 4–8 times higher than that of C1 and C5, with the peak area one order of magnitude larger.

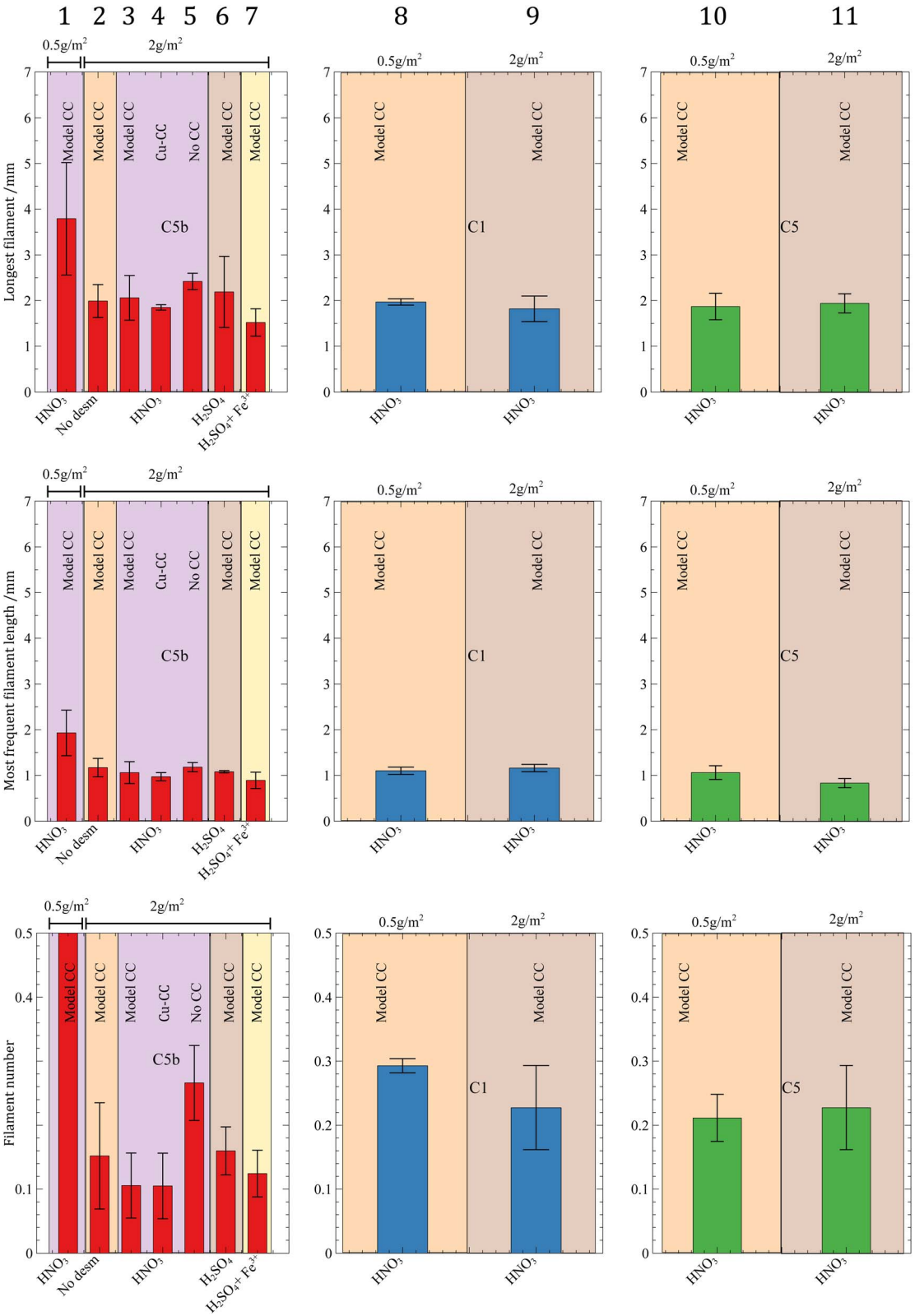

Fig. 2 FFC test results of powder coated 6060 aluminium alloy variants C5b, C1 and C5 (composition in Table 1) after surface pretreatments shown schematically in Fig. 1. The red bar corresponding to the filament number of the variant C5b etched 0.5 g m^{-2} is out of scale because of the very high number of initiation sites on the artificial defect which prevented a precise determination of the number of filaments per unit length. Numbers on the top are used to refer to the different sample sets in the text as defined in Fig. 1.

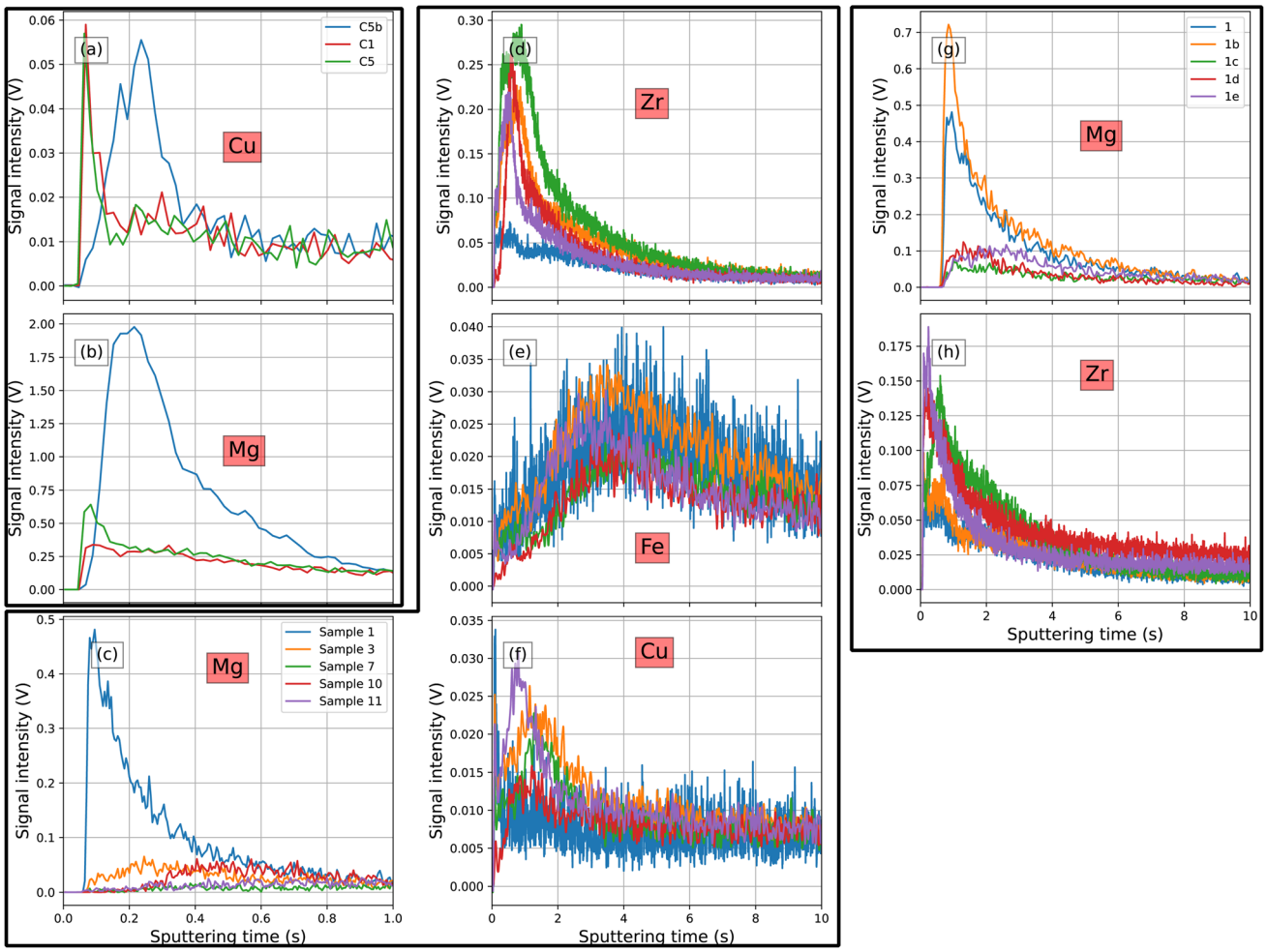

Fig. 3 Elemental depth profiles obtained by GD-OES (signal intensity proportional to concentration; sputtering time proportional to depth) on (a and b) as-received samples and (c–h) after different surface pretreatments and FFC testing. (c–f) After FFC testing and coating removal. (g and h) Different parts of the surface for a sample from set 1. Panels (a) and (b) share the same legend, panels (c–f) share the same legend and panels (g) and (h) share the same legend.

GD-OES analyses for selected samples after FFC testing and coating removal are shown in Fig. 3c–f. These samples were selected to better understand the effect of etching amount and desmutting agent on the surface composition and thus on the FFC susceptibility. The surface concentration of Zr and Mg is comparable for all tested samples except for sample set 1 (0.5 g cm^{-2} etching, HNO_3 desmutting, model-CC) which shows a lower concentration of Zr and a higher enrichment of Mg. The surface enrichment of Cu and Fe is similar for all samples. There is, however, a slightly higher enrichment of Cu on the surface of samples 3, 7 and 11 (2 g cm^{-2} etching, HNO_3 or H_2SO_4/Fe^{3+} desmutting, model-CC). The amount of Zr and Mg present in the near surface region as measured by GD-OES in different spots is shown in Fig. 3g and h. The amount of Zr deposited in different areas of the surface is different. The signal corresponding to the maximum enrichment varies by a factor of 3–4. Samples with lower Mg content displayed high Zr-content, and *vice versa*.

Fig. 4 shows an SEM overview and EDX-based element maps of the surface of samples from sets 1, 3, and 10 (0.5 or 2 g cm^{-2} etching, HNO_3 desmutting, model-CC). Apart from a slightly different surface morphology, no major differences are observed. On the EDX maps of the surfaces, a strong co-location of Zr, Fe, O and Si is observed. Fig. 5 shows HAADF-STEM cross sectional images of selected areas of the surface of samples 1, 3, and 10. Element maps from EELS and EDX are shown in the same image. In all samples, there is a co-location of the signals from Fe, Mn, Si, and Al. Mn, Si and Fe have a strong signal in the same locations on all the three samples, with the exception for sample 3 which in addition shows a region which is only rich in Si. Mg is only present on sample 1 in a region right below the area rich in Zr.

Some of the strongest signals besides those of the dominating aluminium matrix shown in the element maps in Fig. 5 originate from Zr, O and Fe. There is a co-location of Zr and O signals in a thick region on top of the Fe-rich region. A similar thinner co-located region of Zr and O is observed over the aluminium matrix for all three samples.

The apparent presence of a signal from F in the same regions as the signal from Fe is an artifact due to the overlap of the F K-peak with the Fe L-peak. Thus, regions with a strong signal from Fe will seem to have a relatively high signal from F as well.

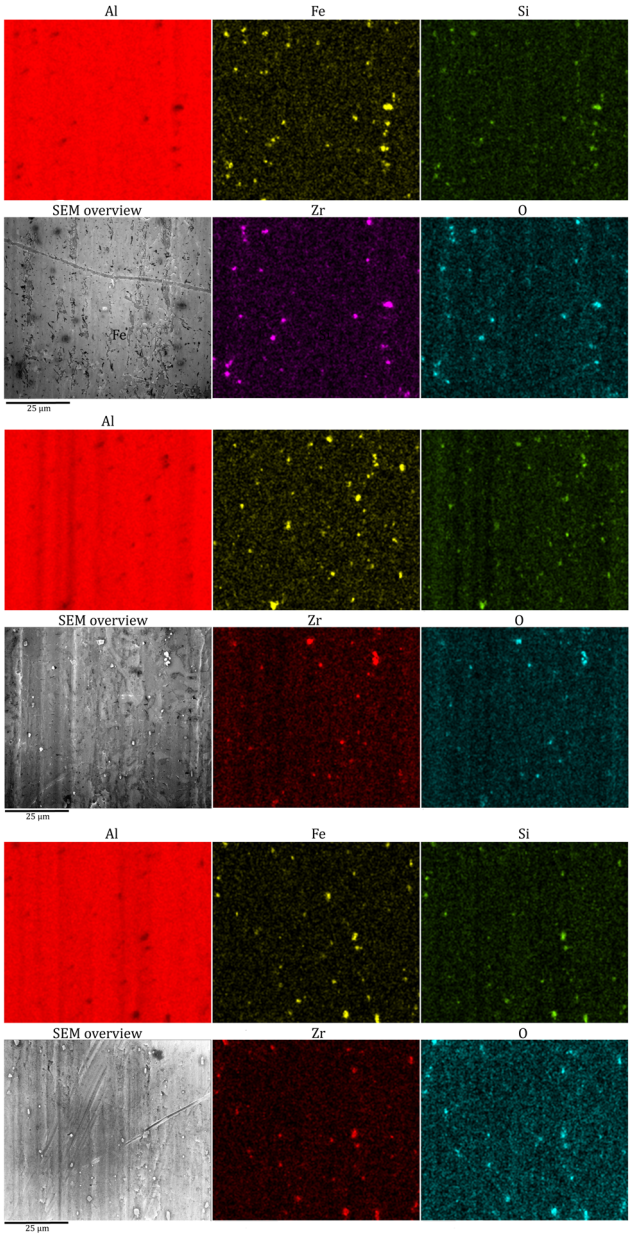

Fig. 4 SEM overview of samples 1, 3, and 10 (from the top bottom), including EDX maps.

However, F is present in other parts of the surface. For sample 1, there is a thin layer of F-based compounds on the very top surface where the presence of aluminium is also observed, and on a thin region in contact with the matrix. For sample 3 the signal from F is more or less uniformly distributed all over the Zr-rich layer present on the top of the Fe-rich region and matrix. For sample 10, the signal from F is below the detection limit.

4 Discussion

4.1 Mg surface enrichment leads to increased FFC susceptibility

The elemental composition and observed microstructural features of the sample surfaces (Fig. 5) are those well-known for aluminium alloys in the 6060 composition window. The Fe-rich noble particles in 6060 alloys are predominantly α-Al(Fe, Mn)Si IMPs,[32] which explains the co-location of the Al, Fe, Mn, and Si signal. The co-location of the signals from Zr and O suggests the formation of a ZrO_2-based conversion layer which is thicker on top of the IMPs for all three samples. The thicker CC on top of the Fe-rich IMPs hints to an increased deposition rate of ZrO_2 on top of these particles.[33] The rate of hydrogen evolution and oxygen reduction on these particles is higher than on aluminium, leading to an increased local pH in these areas. An increased local alkalinity increases the rate of precipitation of ZrO_2-based products which explains the different thickness of the conversion layer in the different regions of the surfaces.[33,34] On a general level, the surface structure and composition described so far are similar to what has been reported in literature for similar systems.[33–37]

The analysis of other elements reveals a very complex interfacial structure. The presence of Mg at the surface of sample 1 (0.5 g cm^{-2} etching, different extrusion plant than sample 10 with equal treatment) indicates the presence of Mg-based oxides. The co-location of the F and Al signals suggests the presence of an Al oxide layer with included flouride on the top and below the ZrO_2. On sample 3 (2 g cm^{-2} etching, otherwise identical to sample 1), Mg is not observed and the presence of F in the same area as the Zr and O suggest the formation of a Zr oxyfluoride conversion layer. In sample 3, there is a stronger F signal intensity both on the top and on the bottom of the Zr-rich region analogously to the situation observed for sample 1. There must be a complex mechanism of formation where the possibility of including F in the structure of the ZrO_2-based conversion products depend on the structure and composition of the surface before the sample is exposed to the conversion bath. On sample 10, F and Mg are below the detection limit. Overlapping barely visible signals of Zr, Al, and O on the outermost part of the surface pointed by the red arrows indicate the presence of a mixture of Zr and Al oxides. Furthermore, the absence of signal in the region between this layer and the matrix indicates that this part of the surface is porous.

The decreased resistance towards FFC of variant C5b sample etched 0.5 g m^{-2} compared to the sample etched 2 g m^{-2} is caused by the incomplete removal of the near surface deformed layer,[38] or the formation of a surface which is not optimal for the subsequent pretreatment steps. The high surface enrichment of Mg detected for variant C5b after FFC tests (Fig. 3) indicates that high amounts of Mg oxides remain on the surface even after the different pretreatment steps when etched for 0.5 g m^{-2}. It is evident from Fig. 3a and b that the surface composition of the as-received samples was different. The high amount of Mg present on the surface of the pristine C5b is not removed by subsequent surface pretreatments. This hypothesis is confirmed by the spectroscopic analysis shown in Fig. 5: sample 1 contains significant amounts of Mg in the region below the conversion film while Mg is below the detection limit for samples 3 and 10. The formation of a non-homogeneous conversion layer on sample 1 can be deduced from Fig. 3g and h where GD-OES measurements are shown for different areas of the same sample. The concentration of Zr is different in the different areas especially when comparing measurements 1

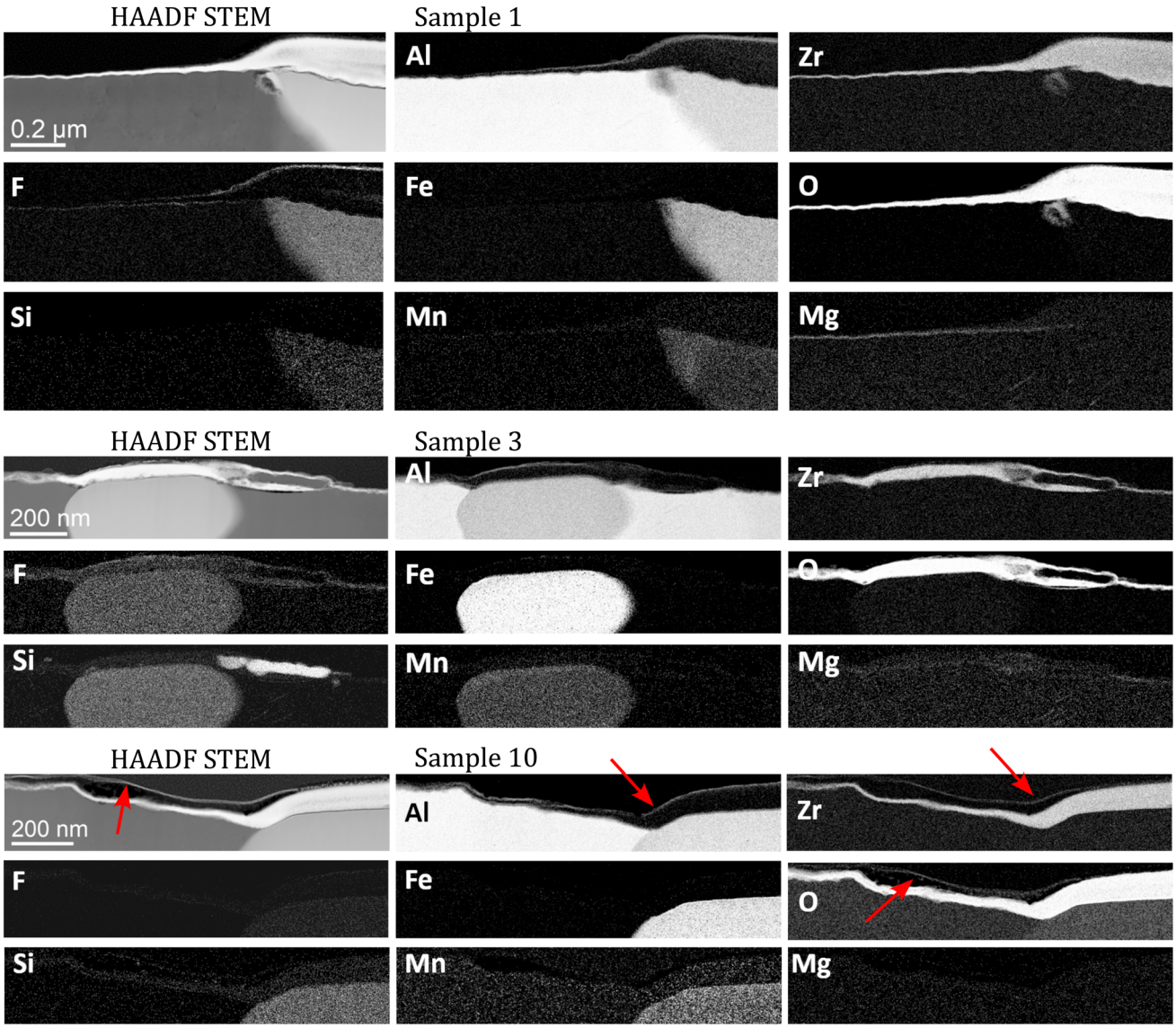

Fig. 5 Images of and elemental distribution in cross sections from samples 1, 3, and 10. HAADF-STEM images as first picture of each series; element maps from EELS and EDX for the respective indicated elements. Red arrows have been added to indicate the presence of a thin layer detached from the surface in certain points.

and 1b with 1c, 1d, and 1e. The formation of a partly porous surface as observed in sample 10 is not reflected in a strongly reduced FFC performance and can not be observed on the larger scale probed by GD-OES.

4.2 Sufficient alkaline etching enables appropriate CC formation

High amounts of Mg on the surface prevent a proper formation of ZrO_2-based conversion coatings, as evidenced by the anti-correlation between the concentration of Mg and Zr (Fig. 3c and e). Samples 3, 7, 10, and 11, which have a comparable surface concentration of Zr, also have a comparable concentration of Mg while sample 1 has a low concentration of Zr and a high concentration of Mg. This anti-correlation hints to the fact that the presence of Mg-(hydr)oxides hinders the formation of a thick and homogeneous ZrO_2-based conversion layer. Fig. 3g and h shows the anti-correlation of the Zr–Mg signals on different areas of sample 1. In addition, the presence of higher and lower concentrations of Zr and Mg on the surface points to the presence of a non-homogeneous conversion coating. This trend cannot be verified by the STEM analysis presented in Fig. 5 as the STEM analysis was performed selecting regions of the surface where the intensity of the Zr signal was the highest. GD-OES, however, shows an averaged concentration profile of a certain element on an area which is orders of magnitude larger than observed in the cross sections so that it is representative of the macroscopic features of a sample.

During alkaline etching, surface enrichment of elements nobler than the matrix takes place on these alloys.[28,29,39] This enrichment has usually a negative impact on the FFC performance.[14] These noble elements usually increase the cathodic activity of the surface and the probability of galvanic coupling

with the less noble aluminium matrix; such coupling is not optimal when it comes to FFC resistance. Comparing Fig. 3d and the FFC test results in Fig. 2 shows that the slightly higher surface enrichment of Cu is not reflected in a higher FFC susceptibility. The absence of such a correlation is especially striking for samples 3 and 7. It has been demonstrated that in certain cases the presence of noble elements such as Cu can be beneficial for the deposition of the conversion layer;[23,37,40] samples alkaline etched without a subsequent desmutting step can have an equal or even better FFC resistance because of the formation of a more homogeneous ZrO_2-based CC.[41] For variant C5b the desmutting step does not have a strong effect on the FFC resistance (comparing sample 2 with 3, 6, and 7 from Fig. 2). Furthermore, the different desmutting solutions lead to relatively small differences in FFC resistance. Only when considering the filament number, hints emerge that a desmutting step could not always have a relevant beneficial effect on the final FFC resistance.

The two ZrO_2 CC variants studied here do not show a great impact on the FFC susceptibility. It is evident from the filiform number in Fig. 2 that the absence of a conversion step leads to a poorer FFC resistance. For sample 1, the presence of only a thin and in certain cases almost absent and heterogeneous conversion film contributes to the poor FFC resistance. The film is clearly evident in Fig. 3g. Since a sample without CC (5) performs better than a sample with an inhomogeneous CC (1), the surface structure and composition formed after the different etching amounts must play an important role not only for the deposition of the conversion film but also on the adhesion properties of the powder coating applied before FFC tests.

4.3 Recycling-related enrichment is not the cause for increased FFC

From the results presented above, it emerges that the most important pretreatment step is alkaline etching. The effect of the subsequent pretreatment steps and the structure and composition of the final surface depend strongly on alkaline etching. With adequate etching conditions, the effect of differences of surface composition of alloys extruded at different production sites or with different amount of alloy elements becomes negligible. The presence of Mg on the surface—most likely in form of (oxy)hydroxides—hinders the formation of a homogeneous conversion layer which in turn has a negative effect on the FFC resistance. Pure acid etching was not investigated in this study, though practised in some plants.

Although it is difficult from the data presented here to picture a full mechanism of formation of the surface layer present on the aluminium matrix before FFC tests, it is clear from GD-OES, HAADF-STEM, and FFC tests that the presence of a higher concentration of Mg combined with a low etching amount leads to the formation of a surface which is more susceptible to the development of a high number of filaments. The cause could be both a reduced adhesion of the organic coating or the high solubility of Mg oxides in acidic environments which are characteristic of the inner part of the filaments.[17,42] However, the incomplete removal of Mg-based products from the surface of variant C5b during the desmutting step in concentrated HNO_3 (Fig. 1) suggests that loss of adhesion is the most plausible initial trigger for larger FFC rates.

5 Conclusion

The FFC resistance depends mainly on the surface pretreatment but the surface structure and composition of the as-extruded samples also have an impact. The presence of magnesium (hydr)oxide interferes with the formation of a thick and homogeneous conversion layer, consequently increasing the FFC susceptibility. Mg surface enrichment cannot be completely removed with 0.5 g m^{-2} of alkaline etching with subsequent desmutting and CC. For the investigated samples, 2 g m^{-2} were sufficient to guaranty the formation of a CC which decreased the FFC susceptibility. Except for the 0.5 g m^{-2} etching condition (for variant C5b), all the investigated surface pretreatments led to FFC susceptibilities well below the accepted industrial requirements. The required etching can be realised with existing processes using existing process chemicals in existing plants. Importantly, the observed Mg enrichment doesn't have a root cause in recycling. Currently, Cu and Zn concentrations of 0.02 wt% are considered the industrial limit; however, appropriate FFC susceptibility can also be achieved at higher concentrations of Cu and Zn using the surface pretreatments investigated during this work. There is also no effect of hitherto unknown impurities. Consequently, novel industrial standards may be required to realise the full potential of PCS-based secondary aluminium; no sudden transitions exist at the upper end of classical composition windows.

Author contributions

Erlind Mysliu: data curation; formal analysis; investigation; writing – original draft; writing – review & editing. John Erik Lein: investigation; methodology. Per Erik Vullum: data curation; formal analysis; investigation; writing – review & editing. Jan Tore Buvik Gundersen: formal analysis; investigation; methodology; resources. Malgorzata Chojak Halseid: conceptualization; funding acquisition; methodology; project administration; resources; supervision; writing – review & editing. Otto Lunder: conceptualization; formal analysis; funding acquisition; methodology; project administration; supervision; writing – review & editing. Andreas Erbe: conceptualization; funding acquisition; methodology; resources; supervision; writing – review & editing.

Conflicts of interest

J. T. B. G. and M. C. H. are employees of a company with commercial interests in increased use of recycled aluminium. P. E. V., M. C. H., O. L. and A. E. have a wide academic and industrial network and a number of research activities beyond this manuscript which may be related to the topic to a certain degree.

Data availability

Research data is available *via* NTNU's institutional dataverse repository at https://doi.org/10.18710/B9EJM8.

Acknowledgements

This work was supported by the Research Council of Norway (NFR), innovation project for the industrial sector CORAL, grant number 309875, with support from the industrial partners Hydro and Speira. Support from the Research Council of Norway through the infrastructure projects NORTEM (197405) and NorFab (295864) is gratefully acknowledged. We acknowledge Anita Storsve, Marthe Folstad and the NTNU Fine-mechanical Workshop for technical assistance.

Notes and references

1 European Aluminium, *Environmental profile report for the aluminium refining industry*, 2021, https://european-aluminium.eu/blog/enabling-the-circular-economy-with-aluminium/, accessed 2024-07-22.
2 A. Lennon, M. Lunardi, B. Hallam and P. R. Dias, *Nat. Sustainability*, 2022, **5**, 357–363.
3 C. Radlbeck, E. Dienes and D. Kosteas, *Struct. Eng. Int.*, 2006, **16**, 339–344.
4 G. Liu and D. B. Müller, *Environ. Sci. Technol.*, 2013, **47**, 4882–4888.
5 S. S. Panigrahi, S. Mishra and B. Sahu, *Environ. Dev. Sustain.*, 2025, **27**, 14469–14495.
6 D. Raabe, D. Ponge, P. J. Uggowitzer, M. Roscher, M. Paolantonio, C. Liu, H. Antrekowitsch, E. Kozeschnik, D. Seidmann, B. Gault, F. De Geuser, A. Deschamps, C. Hutchinson, C. Liu, Z. Li, P. Prangnell, J. Robson, P. Shanthraj, S. Vakili, C. Sinclair, L. Bourgeois and S. Pogatscher, *Prog. Mater. Sci.*, 2022, **128**, 100947.
7 G. Jarrín Jácome, M. F. Godoy León, R. A. F. Alvarenga and J. Dewulf, *Resources*, 2021, **10**, 72.
8 R. Lin, B. Liu, J. Zhang and S. Zhang, *J. Mater. Res. Technol.*, 2022, **19**, 354–367.
9 S. Tjøtta, L. Dardinier and B. Kurth, *Aluminium Extrusion and Finishing*, 2020, pp. 18–24.
10 S. Tjøtta, L. Dardinier, G. Rombach and R. Scharf-Bergmann, *Proceedings of the Twelfth International Aluminium Extrusion Technology Seminar & Exposition*, Wauconda, IL, USA, 2022, p. MI39.
11 I. Park, M. Ito, S. Jeon, C. B. Tabelin, T. Phengsaart, M. Silwamba and N. Hiroyoshi, *Miner. Eng.*, 2023, **201**, 108202.
12 E. H. Bartawi, C. D. Marioara, G. Shaban, C. Hatzoglou, R. Holmestad and R. Ambat, *ACS Nano*, 2023, **17**, 24115–24129.
13 Z. C. Sims, H. B. Henderson, M. J. Thompson, R. P. Chaudhary, J. A. Hammons, J. Ilavsky, D. Weiss, K. Anderson, R. Ott and O. Rios, *Eur. J. Mater.*, 2021, **1**, 3–18.
14 A. Afseth, J. H. Nordlien, G. M. Scamans and K. Nisancioglu, *Corros. Sci.*, 2002, **44**, 2529–2542.
15 E. Mysliu, I. Taji and A. Erbe, *RSC Appl. Interfaces*, 2025, **2**, 304–319.
16 H. N. McMurray and G. Williams, in *Shreir's Corrosion*, Elsevier, Oxford, 2010, pp. 988–1004.
17 E. Mysliu, O. Lunder and A. Erbe, *Phys. Chem. Chem. Phys.*, 2023, **25**, 11845–11857.
18 K. Raviprabha, R. S. Bhat, S. I. Bhat, P. Nagaraj and K. Jyothi, *Heliyon*, 2023, **9**, e16036.
19 P. Premendra, H. Terryn, J. M. C. Mol, J. H. W. de Wit and L. Katgerman, *Mater. Corros.*, 2009, **60**, 399–406.
20 C. Senöz and M. Rohwerder, *Electrochim. Acta*, 2011, **56**, 9588–9595.
21 C. Senöz, S. Borodin, M. Stratmann and M. Rohwerder, *Corros. Sci.*, 2012, **58**, 307–314.
22 H. Zhao, Y. Yin, Y. Wu, S. Zhang, A. M. Mingers, D. Ponge, B. Gault, M. Rohwerder and D. Raabe, *Nat. Commun.*, 2024, **15**, 561.
23 E. Mysliu, K. Sletteberg Storli, H. M. Skogøy, S. Kubowicz, I.-H. Svenum, O. Lunder and A. Erbe, *Electrochim. Acta*, 2024, **477**, 143805.
24 B. J. M. Freitas, G. Y. Koga, M. A. B. Mendes, C. S. Kiminami, W. J. Botta and C. Bolfarini, *Metall. Mater. Trans. B*, 2023, **54**, 2188–2205.
25 M. Safyari, A. Bendo and M. Moshtaghi, *Mater. Today Commun.*, 2024, **38**, 108390.
26 J. Kim, S. Shin and S. Lee, *Mater. Charact.*, 2022, **193**, 112276.
27 A. Lutz, M. C. Halseid and I. D. Graeve, *Mater. Corros.*, 2022, **73**, 1575–1585.
28 M. Halseid, J. T. B. Gundersen, Ø. Bauger and T. Hentschel, *Surf. Interface Anal.*, 2019, **51**, 1225–1230.
29 E. Mysliu, K. S. Storli, E. Kjørsvik, O. Lunder and A. Erbe, *J. Electrochem. Soc.*, 2023, **170**, 011503.
30 Qualicoat, *Qualicoat Specifications*, 2021, https://www.qualicoat.net/main/specifications.html.
31 E. Mysliu, J. E. Lein, P. E. Vullum, J. T. Buvik Gundersen, M. Chojak Halseid, O. Lunder, A. Erbe, Replication data for: "Primary-equivalent corrosion protection of post-consumer scrap based aluminium", NTNU Open Research Data, 2025, DOI: 10.18710/B9EJM8.
32 L. F. Mondolfo, *Aluminum Alloys*, Butterworth-Heinemann, London, UK, 1976, pp. 661–663.
33 O. Lunder, C. Simensen, Y. Yu and K. Nisancioglu, *Surf. Coat. Technol.*, 2004, **184**, 278–290.
34 F. Andreatta, A. Turco, I. de Graeve, H. Terryn, J. H. W. de Wit and L. Fedrizzi, *Surf. Coat. Technol.*, 2007, **201**, 7668–7685.
35 J. H. Nordlien, J. C. Walmsley, H. Østerberg and K. Nisancioglu, *Surf. Coat. Technol.*, 2002, **153**, 72–78.
36 P. Bouckenooge, O. Bauer, K. Eckhard and H. Terryn, *Surf. Interface Anal.*, 2020, **52**, 174–184.
37 A. Sarfraz, R. Posner, M. Lange, K. Lill and A. Erbe, *J. Electrochem. Soc.*, 2014, **161**, C509–C516.
38 J. H. Nordlien, J. Defrancq, W. Züst, M. Benmalek and R. Stuckart, *Mater. Corros.*, 2000, **51**, 473–480.
39 H. Leth-Olsen and K. Nisancioglu, *Corros. Sci.*, 1998, **40**, 1179–1194.
40 S. Adhikari, K. A. Unocic, Y. Zhai, G. S. Frankel, J. Zimmerman and W. Fristad, *Electrochim. Acta*, 2011, **56**, 1912–1924.
41 C. F. Glover, M. L. C. Lim and J. R. Scully, *Corrosion*, 2020, **77**, 40–52.
42 P. P. Leblanc and G. S. Frankel, *J. Electrochem. Soc.*, 2004, **151**, B105.